IEEE Access
Multidisciplinary | Rapid Review | Open Access Journal

Received 2 January 2024, accepted 18 January 2024, date of publication 23 January 2024, date of current version 1 February 2024.

Digital Object Identifier 10.1109/ACCESS.2024.3357488

RESEARCH ARTICLE

Miniaturized Dual Band Implantable Antenna for Implanted Biomedical Devices

ABDENASSER LAMKADDEM[1], AHMED EL YOUSFI[1], VICENTE GONZÁLEZ-POSADAS[2], AND DANIEL SEGOVIA-VARGAS[1], (Senior Member, IEEE)

[1]Signal Theory and Communications Department, Carlos III University of Madrid, 28911 Madrid, Spain
[2]Signal Theory and Communications Department, Polytechnic University of Madrid, 28040 Madrid, Spain

Corresponding author: Abdenasser Lamkaddem (abdenasser@tsc.uc3m.es)

This work was supported in part by the U.S. Department of Commerce under Grant BS123456.

ABSTRACT In this paper, we present a novel design of a compact miniaturized dual-band antenna for industrial, scientific, and medical (ISM) implantable applications working at 915 MHz and 2.4 GHz. The proposed antenna has a compact size of ($6 \times 6 \times 0.25$ mm^3). The antenna shows a wide bandwidth of 12.6 % at the lowest frequency and 12.8 % at the highest frequency and gain values of -21.8 dBi and -19.2 dBi at 915 MHz and 2.4 GHz, respectively which are relatively high for implantable applications. The design has been done for healthy and unhealthy tissues (adenocarcinoma). Furthermore, the fabricated prototype has been tested in minced pork as a suitable real tissue to validate the simulated results. Finally, a comparison with the recently published state-of-the-art solutions is provided showing good results in terms of size, bandwidth and gain.

INDEX TERMS Dual band, frequency-independent antenna, implantable antenna, industrial, scientific, and medical (ISM) bands, miniaturization.

I. INTRODUCTION

In recent years, the use of wireless implantable medical devices (WIMD's) has experienced a significant increase in health monitoring, hyperthermia, and cancer detection [1], [2], [3]. Diseases such as the incidence of esophageal adenocarcinoma have rapidly increased over the past few decades [4]. However, until now, implantable antenna inside adenocarcinoma has never been considered, due to the lack of actual dielectric properties of this kind of tissue. Recently, in [5], the authors succeeded in the measurements of the dielectric properties of the adenocarcinoma, which gives us the possibility to study implantable antennas inside the unhealthy small intestine for the first time.

The implantable antenna is a key component for the WIMD's, since it ensures communication with the external devices. According to [5] the frequency dependence of the electrical parameters of healthy and unhealthy tissues makes reasonable that implantable antennas may have, at least, broadband or dual-frequency performance. In addition, physical requirements such as space limitation, the lifetime of the battery, ease of fabrication and, the patient safety are key factors in WIMD's. Then, when dealing with implantable antennas, it's crucial to concurrently address three primary objectives which are miniaturization, multiband or wideband performance to avoid detuning effects due to the change of tissue environments.

Concerning the wideband performance, several applications can be recently found in literature. Among them, different technologies can be mentioned such as a wideband folded dipole antenna working from 700 to 2194 MHz [6], a circularly polarized patch antenna working at 2.45 GHz [7], a dual-band patch antenna working at 400 MHz and 2.45 GHz [8] and a dual-band planar inverted F-antenna (PIFA) operating in medical device radiocommunications (MedRadio) band at 400 MHz and ISM band at 915 MHz [9]. However, all of them had large dimensions (in the order of an average 2 $\times$ 2 cm^2) what made them difficult to be used as implantable antennas.

Then, the second bottle-neck to be overcome is the miniaturization degree. According to [10] the upper limit for the device size would not be larger than 2 % of the host body

The associate editor coordinating the review of this manuscript and approving it for publication was Masood Ur-Rehman.

size. The most common techniques to miniaturize antennas, down to the required limit, are either the addition of shorting pins or, the use of high permittivity substrates or the inclusion of meandered lines or the inclusion of open-end slots in ground plane. Then, a compact implantable antenna was designed for pacemaker devices in [11]. However, the single band behaviour and the thickness of 1.27 mm is the major drawbacks to work as implantable antennas. In [12] a single band fully planar antenna based on complementary split-ring resonator was printed on a high permittivity substrate for 2.45 GHz applications. The antenna was fully planar with a non-negligible impedance bandwidth (up to 12.2%) and presented a small enough size ($8.5 \times 8.5 \times 1.27$ mm^3) to be considered as an implantable device. However, the gain of the antenna is low (around -24.3 dBi) and the fact that it only covered one frequency band made the device difficult to be used when potential detuning could appear. In [13] a patch antenna with multiple slots and one shorting pin was proposed to achieve one single-band antenna for a wireless capsule endoscope system. The thickness of the antenna is 1.27 mm, the low gain of -28.7 dBi, and the single-band performance making it not-suitable for this kind of application. In [14] a dual-band implantable patch antenna ($7 \times 7.2 \times 0.2$ mm^3) sized was presented for (ISM) bands (920 MHz and 2.45 GHz). The limited gain of -28.7 dBi at 920 MHz, and -25.6 dBi at 2.45 GHz, besides the presence of shorting pins and a defected ground plane made the fabrication process more complex and sensitive.

Recently, in [15] a first attempt to make a fully planar and dual-band implantable antenna was done by introducing a meandered line PIFA antenna with some kind of metamaterial structure acting as a superstrate. Despite its great performance in terms of size ($7 \times 6 \times 0.5$ mm^3) and gain, it still needed shorting pins and an outer cover to isolate the metasurface from the inner what converted the antenna into some bulky device ($14 \times 8 \times 5$ mm^3). A second meandered structure was proposed in [16] to achieve a tri-band implantable antenna. It still needed some shorting pins and was somewhat bulky ($19 \times 15 \times 0.25$ mm^3). Finally, a thick 2.54 mm implantable antenna was presented in [17] but its thickness could make it unsuitable for some applications.

A fully planar and single layer implantable antenna with no shorting pins for ISM applications is presented in this paper. The key factors in the design of the implanted antenna are the inclusion on a patch antenna of an arrangement of slots that maximizes the gain allowing larger link ranges while keeping a miniaturized size. A loop shaped structure (to achieve a dual frequency performance) has also been added. The dimensions of the proposed dual-band implantable antenna are ($6 \times 6 \times 0.25$ mm^3). The key features of the antenna are its small size, dual-band, single layer, and independency between the highest and the lowest frequency. Finally, the proposed antenna was initially analysed inside a 45 mm depth of a homogeneous muscle box. Subsequently, to imitate the simulation real scenario, minced pork is used for the measurements. The electrical properties of pork [18], exhibit similarities to muscle modelled at frequencies of 915 MHz and 2.45 GHz.

The rest of this paper is organized as follows. Section II provides the antenna design geometry, the medium under study, the equivalent model circuit, and the parameters of the components. Followed by a comparison between simulated and measured results in Section III. Finally, the paper concludes in Section III.

II. ANTENNA DESIGN

A. CONFIGURATION

The proposed antenna geometry is shown in Fig. 1. The radiating element consists of a patch antenna with a slotted meandered line designed for the 915 MHz band and a simple ring for the 2.4 GHz band as shown in Fig. 1(a). The antenna has been printed on Rogers RO3010 substrate material of permittivity 10.2 and loss tangent of 0.0035. The design remains simple and compact, it has a size of ($6 \times 6 \times 0.25$ mm^3) and a full ground plane as depicted in Fig. 1(b). The profile of the antenna has been reduced by a factor of 10 (compared to [19]) resulting in a fully suitable implantable antenna structure. Table 1 summarizes the detailed parameters of the proposed antenna.

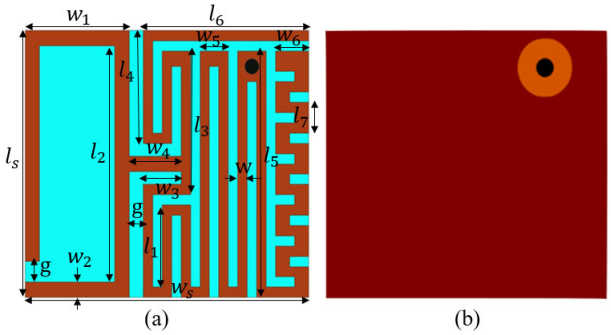

FIGURE 1. The geometry of the antenna design (a) Front view (b) Bottom view.

TABLE 1. Values of the antenna parameters.

Symbol	w_s	l_s	g	w	l_6	w_2	w_3	w_4	l_1
Value [mm]	6	6	0.3	0.2	3.5	0.3	0.8	1.1	1.8
Symbol	l_7	l_4	w_5	w_6	w_1	l_3	l_5	l_2	
Value [mm]	0.6	2.8	0.7	0.8	2.2	3	5.6	5.4	

B. SIMULATION ENVIRONMENT

The objective of this section is to characterize the properties of the human body medium, which is used to simulate the proposed implantable antenna. Using the Debye model expressions and the experiments data provided in [5] and [20], the plot of the dielectric properties of different human tissues versus frequency are shown in Fig. 2. The stomach has the highest permittivity from 66 to 62 because of the high water content and a conductivity from 1.1 to 2.6 S/m in the frequency range between 600 MHz and 3 GHz. This is

followed by the adenocarcinoma, which has a permittivity between 64.5 and 59.5 and a conductivity from 1.1 to 2.6 S/m. The small intestine has a permittivity between 62 and 53.5 and a conductivity from 2 to 3.6 S/m. The kidney has a permittivity between 62 and 52 and a conductivity from 1.25 to 2.75 S/m. The small intestine lumen has a permittivity between 56 and 53 and a conductivity from 0.8 to 2.1 S/m. Finally, grey brain matter exhibits the smallest permittivity and conductivity between 55 and 48 and from 0.8 to 2.15 S/m respectively due to the low water content. A three-layered

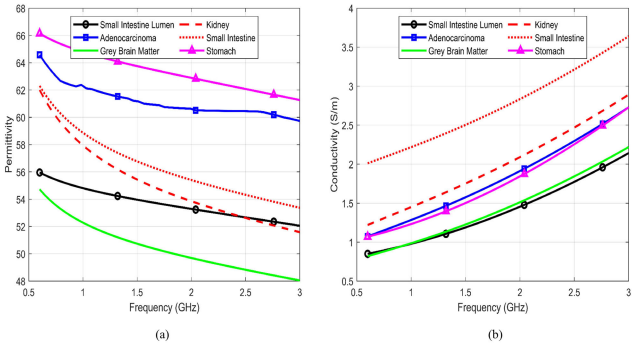

FIGURE 2. Dielectric-properties of the human tissues versus frequency. (a) Relative permittivity. (b) Conductivity.

body phantom of dimensions (80 × 80 × 60 mm^3) was used for the simulations as shown in Fig. 3. The properties of the tissue conductivity and permittivity were adjusted to be frequency-dependent for the entire band used in the simulation. The antenna was simulated in a depth of 45 mm inside the body phantom.

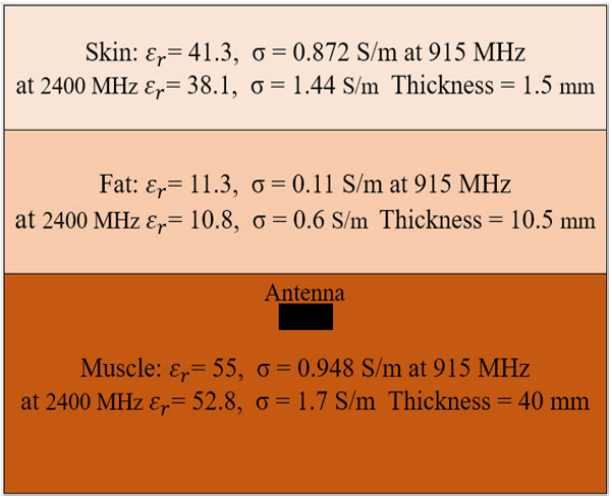

FIGURE 3. The proposed antenna implantation within a three-layered phantom at 45 mm depth.

C. WORKING PRINCIPLE AND PARAMETRIC STUDY

The design steps (1,2,3) of the proposed antenna are shown in Fig. 4. Due to the complexity of the antenna, in parallel with the antenna design an equivalent circuit has been developed to better understand any of the elements of the antenna.

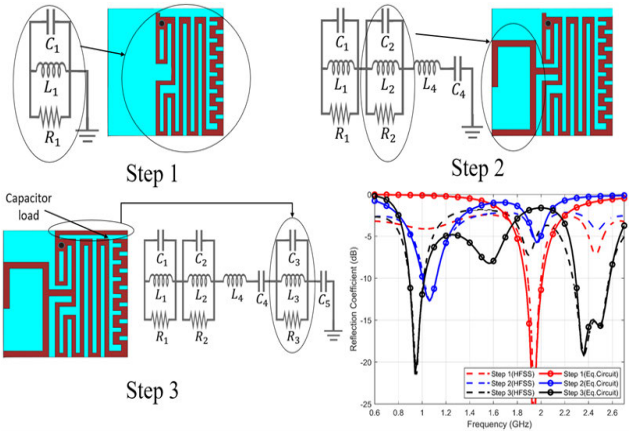

FIGURE 4. Optimization steps for the proposed antenna and the corresponding $|S_{11}|$.

Firstly, we designed a meandered line for the lower band; the $|S_{11}|$ of step 1 was resonating at 1.9 GHz, which is modeled by the first resonator C_1, L_1, and R_1. Secondly, in step 2 a simple ring was added for dual-band performances; the ring shifted the first resonate frequency to 1 GHz, and it is modelled by C_2, L_2, and R_2 in the equivalent circuit. Moreover, the coupling between the meander line and the ring is represented by C_4 and L_4. Finally, not only the added arm to the top of the meandered line help to achieve the desired bands and impedance matching but also creates a new band from 2.4 GHz to 2.57 GHz. This enhances the bandwidth in the highest band. The arm at the top of the meandered line is presented by C_3, L_3 and R_3 as presented in step 3, C_5 = 1.7 pF is the loaded capacitor when the antenna is capacitively loaded (The capacitive load is caused by adding the line to the top of the meander line, which creates a capacitor load between the meander line and the top arm). In addition, a lumped equivalent circuit has been proposed to identify the proposed antenna and estimate the resonant frequencies as shown in Fig. 5. 1, 2, and 3 are representing the three different design sections which are meandered line, ring, and added arm respectively. As a result, the dual-band is achieved ($|S_{11}| \leq -10$ dB) for both ISM bands from 890 MHz to 1 GHz and from 2.26 GHz to 2.57 GHz.

The final equivalent circuit model is detailed in Fig. 5. C_p and L_p are the capacitance and the inductance of the coaxial cable, respectively.

The right side of the antenna is a meandered line (Fig. 6), to calculate the inductance of the meander line we use the method described in [21] and [22]. This method is based on the measured data and a monomial expression which includes all the meander line variables. The monomial expression is:

$$L_1 = 0.00266\, a^{0.0603} l_5^{0.4429} N^{0.954} d^{0.606} w^{-0.173} \quad (1)$$

where, (N) represents the number of segments of the meandered line, (a = w_4, b = l_4, d = w_5, w) and (l_5) are shown in Fig. 6.

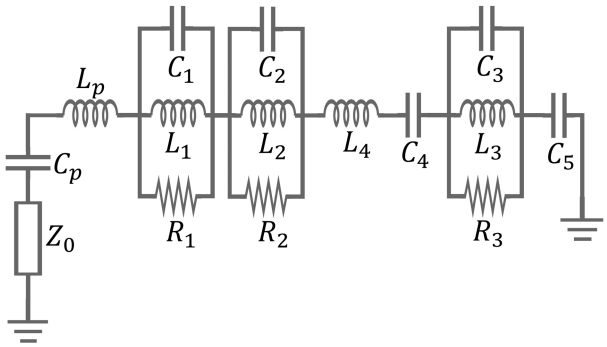

FIGURE 5. Proposed equivalent circuit of the antenna design.

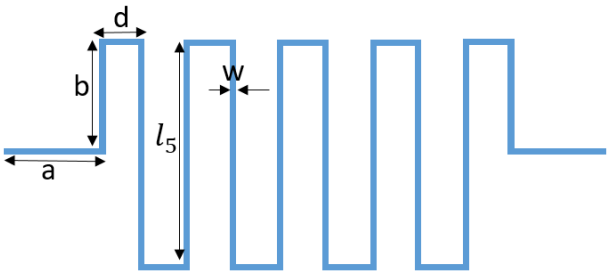

FIGURE 6. The geometry of the meander line.

The capacitance C_1 of the meander line is calculated by the expression referred to [23] by:

$$C_1 = l_{tot}[\epsilon_0\epsilon_r \frac{2\pi}{ln(1+\frac{2l_5}{t}+\sqrt{\frac{2l_5}{t(\frac{2l_5}{t+2})}})} + \epsilon_0\epsilon_r \frac{w-\frac{t}{2}}{l_5}] \quad (2)$$

where: (l_{tot}) is the total length of the meandered line, (t) is the thickness of the meandered line and (l_5) is the length of the segments of the meandered line. Using the optimized values for the proposed antenna (Table 1), the estimated L_1 and C_1 are 4.73 nH and 6.16 pF respectively. On the left side of our design, we have a simple rectangular ring, which has an LC equivalent circuit. The values of C_2 and L_2 can be calculated using the expressions reported in [24] and [25] respectively.

$$C_2 = \frac{(\pi l_2 - g)C_{pul}}{2} + \frac{\epsilon_0 w_2 t}{2g} \quad (3)$$

$$L_2 = 0.0002l_2(2.303log_{10}\frac{4l_2}{w_2} - \gamma) \quad (4)$$

where (l_2) is the length total of the ring, g is the gap, C_{pul} is the capacitance per unit length, (w_2) is the width of the ring segment, (t) is the thickness of the ring, (γ) is a constant depends on the geometry of the ring. $C_5 = 1.7$ pF is the loaded capacitor when the antenna is capacitively loaded [6]. Table 2 summarizes the circuit model parameters. The proposed antenna exhibits dual-band performance. The comparison between simulation and the equivalent circuit is shown in Fig. 7. Good agreement can be seen between the simulation and the equivalent circuit model.

Fig. 8 shows the simulation for three different lumped elements cases. The values for each situation are detailed in Table 3. All the values are constant except those of the tuning stub (C3, L3, and R3). Increasing L3 from 1.33 to 1.478 while decreasing C3 from 5.22 to 3.86, only shifts the second frequency band to lower frequencies, without any significant modification in the first frequency band. This indicates that C3, L3, and R3, are the only parameters that affects the highest frequency band, which leads to enhancing the bandwidth.

TABLE 2. Values of the circuit model parameters (Units: Ω, *nH*, *pF*).

Symbol	C_1	L_1	R_1	C_2	L_2	R_2	C_3	L_3
Value	3.62	5.54	143	13.82	0.31	54.3	3.86	1.47
Symbol	R_3	C_4	L_4	C_5	C_p	L_p	Z_0	
Value	431	3.97	8.77	1.7	98	0.237	50	

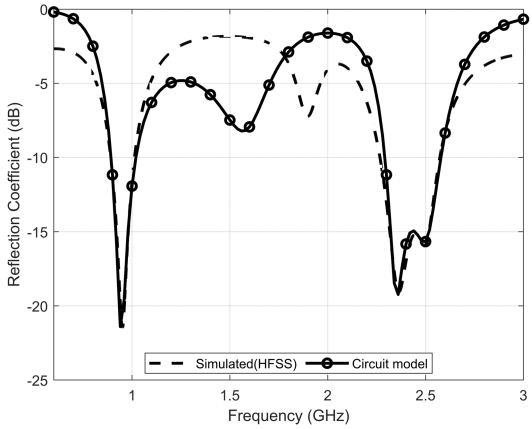

FIGURE 7. Comparison of the simulated and circuit model of the proposed antenna.

TABLE 3. Values of the circuit model CASES(D,E,F) (Units: Ω, *nH*, *pF*).

Symbol	C_1	L_1	R_1	C_2	L_2	R_2	C_3	L_3	R_3
CASE D	3.6	5.5	143	13.8	0.3	54	5.2	1.3	5k
CASE E	3.6	5.5	143	13.8	0.3	51	4.54	1.44	9k
CASE F	3.6	5.5	143	13.8	0.3	54	3.86	1.47	431

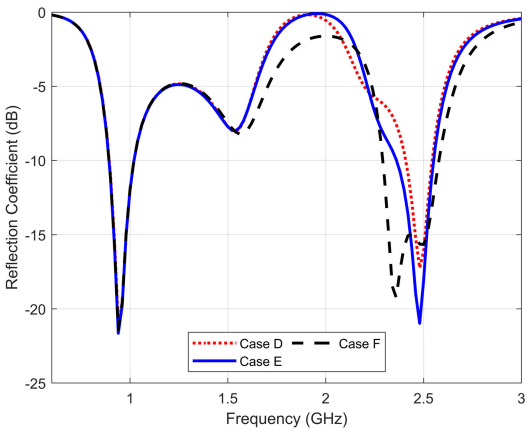

FIGURE 8. $|S_{11}|$ of different lumped elements CASES(D,E,F).

In the same way, we made C3, L3, and R3 values be constant, and we study the variation of the other elements as

shown in Table 4. Increasing L1 from 2.88 to 5.54 while, with decreasing C1 from 6.6 to 3.6, shifts the lowest frequency band from 1 GHz to 915 MHz. On the other hand, increasing C2 from 10 to 13.8, with decreasing L2 from 0.39 to 0.3, shifts the highest frequency to the left sidelower ones, and improves the matching at the lowest frequency, without changing its highest frequency (Fig. 9).

TABLE 4. Values of the circuit model CASES(A,B,C) (Units: Ω, *nH*, *pF*).

Symbol	C_1	L_1	R_1	C_2	L_2	R_2	C_3	L_3	R_3
CASE A	6.6	2.8	129	13.82	0.31	87	3.86	1.47	5k
CASE B	3.9	5.5	135	10	0.39	62	3.5	1.48	1k
CASE C	3.6	5.5	143	13.82	0.31	54	3.86	1.47	431

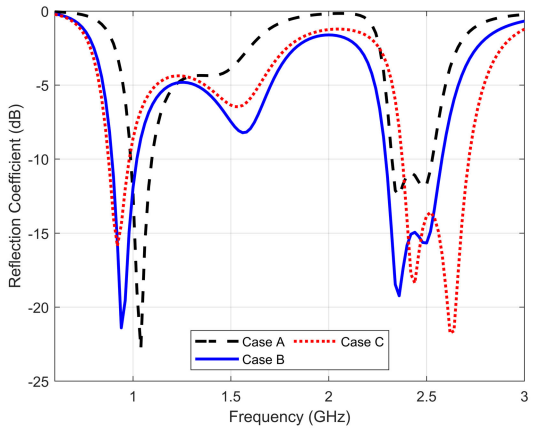

FIGURE 9. $|S_{11}|$ **of different lumped elements CASES(A,B,C).**

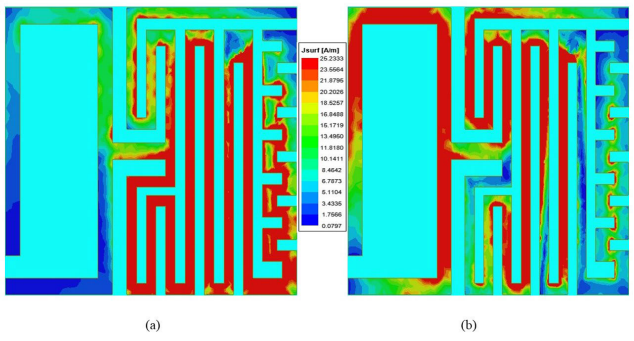

FIGURE 10. Current distributions of the proposed antenna at. (a) 915 MHz. (b) 2.4 GHz.

The working principle of this dual band antenna can be explained by showing the current distribution at the operating frequencies (Fig. 10). At 915 MHz (Fig. 10(a)), the maximum current density is placed along the meander line, with a current null at the left rectangular loop. This makes the meander line responsible for the radiation at the 915 MHz frequency band. It is worth noting that the additional meander line section at the right edge of the antenna increases the antenna electrical length more, by increasing the number of turns, without increasing its physical length. Consequently, it helps reducing the lowest resonant frequency. On the other hand, the current distribution at 2.4 GHz resonant frequency can be seen in (Fig. 10(b)). It can be appreciated that, at 2.4 GHz, the maximum current density is mainly placed on the rectangular loop, some on the arm placed over the meander line and, finally, another part of the current at the left part of the meander line. The overall effect of this current distribution provoked a relatively broad band centred at 2.4 GHz. The effect of the arm placed on the top of the meander line will be discussed on the next paragraph.

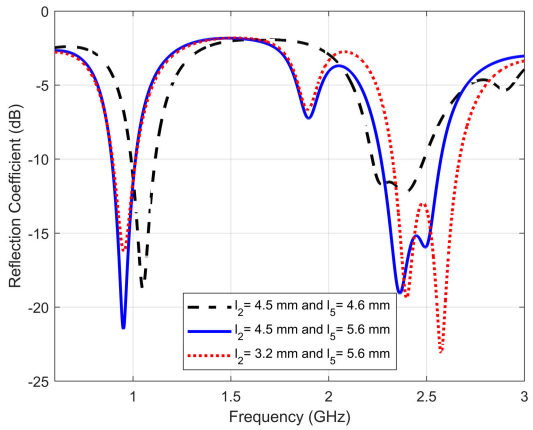

FIGURE 11. Parametric study of the proposed antenna as a function of the length of meandered line and the ring.

Finally a parameter study is included to better understand the antenna behaviour. The effect of the length of the meandered line (l_5) and the length of the ring (l_2) is shown in Fig. 11. An increase in the length (l_5) from 4.6 mm (dashed black line) to 5.6 mm (solid blue line) decreases the lowest frequency without hardly affecting the higher operating band. On the other hand, increasing the length (l_2) from 3.2 mm (dashed red line) to 4.5 mm (solid blue line) decreases the higher operating band without affecting the lowest frequency which emphasizes the frequency-independent behavior of the proposed antenna.

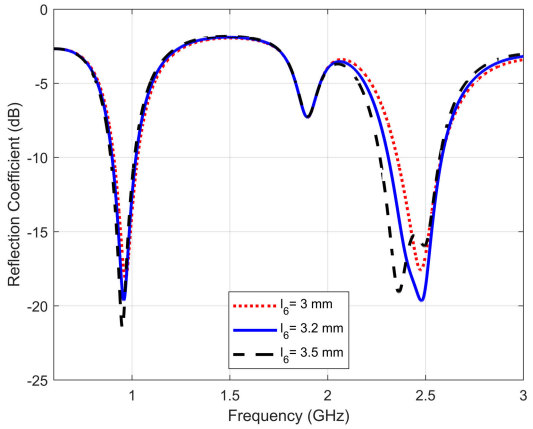

FIGURE 12. Parametric study of the proposed antenna as a function of the arm length (l_6).

The effect of the length (l_6) is studied with the help of Fig. 12 and of the current distribution shown in Fig. 10. The

arm at the top of the meandered line with length (l_6) works as a tuning stub. 915 MHz band is mainly excited along the meandered line without neither the tuning stub nor the C-structure contributions. On the other hand, the tuning stub has a significant role in exciting the second and the third frequency band. In that way, an electromagnetic coupling appears between the tuning stub and the meandered line, which creates a new frequency band around 2.5 GHz. Taking advantage of the newest frequency band created by the tuning stub we can easily increase the tuning stub length (l_6) to increase the current path. Increasing (l_6) up to 3.5 mm results in a wider bandwidth at the higher frequency from 2.26 to 2.57 GHz as showed in Fig. 12. The current distribution shown in Fig. 10 indicates a broadening of the highest frequency band without affecting the lowest band.

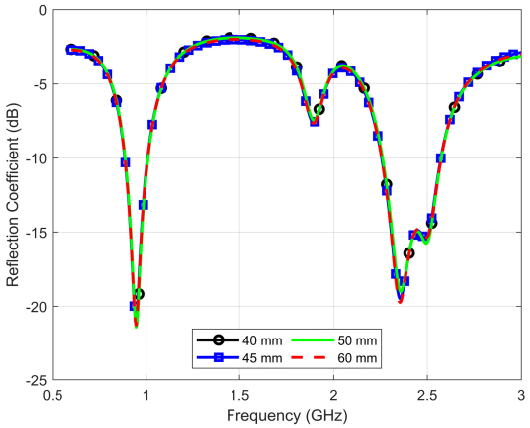

FIGURE 13. Simulated $|S_{11}|$ for different depths.

Fig. 13 displays the simulated $|S_{11}|$ for different depths. $|S_{11}|$ is depicted for depth values of 40mm, 45mm, 50mm, and 60mm. The findings indicate the antenna meets specifications ($|S_{11}| < -10$dB) along all implantation depths (Fig. 13). This suggests that implanting the antenna at different depths within the tissue doesn't impact the impedance matching or resonance frequency. Thus, the antenna's sensitivity remains unaffected by the depth of implantation.

Introducing a capsule with the circuitry components (Helix, Electrode, Holder, Antenna, PCB, batteries, Lid, Biocompatible shield) that has been designed as illustrated in Fig. 14.

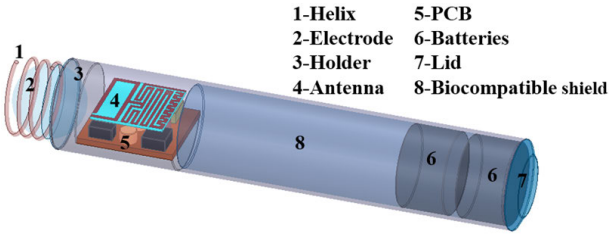

FIGURE 14. Capsule with the circuitry components.

The simulated $|S_{11}|$ of the proposed antenna with capsule is very similar to the simulated one without capsule as shown in Fig. 15.

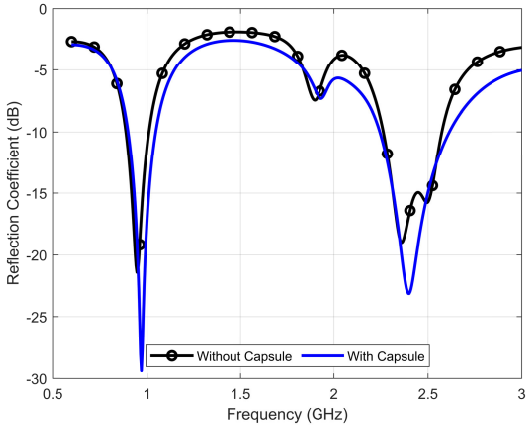

FIGURE 15. Simulated |S11| of the proposed antenna with and without capsule.

Fig. 15 illustrates the simulated $|S_{11}|$ with and without the capsule and other electronic components. Results indicate that the antenna meets the specifications ($|S_{11}| < -10$dB) in both scenarios, as depicted in Fig. 15. The capsule doesn't impact the impedance matching or resonance frequency, implying that the antenna's sensitivity remains unaffected by its presence.

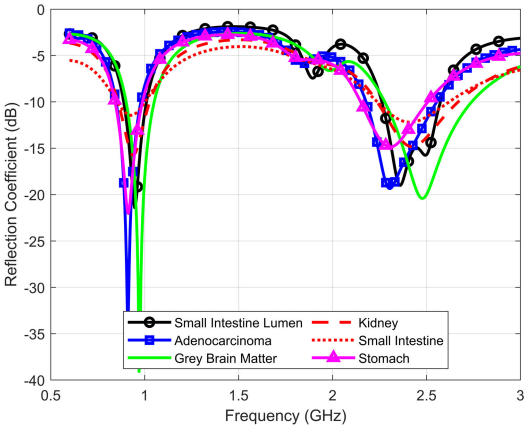

FIGURE 16. $|S_{11}|$ comparison in different tissue types.

Fig. 16 shows the $|S_{11}|$ of the proposed antenna inside different tissue types. It can be observed that the proposed antenna satisfies the -10 dB requirement between 890 MHz and 1 GHz and from 2.26 to 2.57 GHz inside small intestine lumen. Inside adenocarcinoma the $|S_{11}|$ has been shifted to the left side and has a good impedance matching in the lowest frequency band from 845 to 980 MHz and exhibits a wider bandwidth from 2.17 to 2.55 in the highest frequency band. This is due to the fact that that the permittivity of adenocarcinoma is much larger at both frequencies than the one of grey matter (Fig. 2). This will shift down the frequency more in the presence of adenocarcinoma than in the presence

of grey matter. In addition, as the losses are also greater, the bandwidth associated to adenocarcinoma will be larger than the one associated to grey matter. It is worth noting that the losses are more sensitive to highest frequencies than to lowest ones. Moreover, the antenna has been tested inside the small intestine and it has a $|S_{11}|$ from 854 MHz to 1 GHz and from 2.24 to 2.61 GHz. Furthermore, the $|S_{11}|$ inside stomach is between 845 and 989 MHz and from 2.14 to 2.5 GHz. Inside kidney the $|S_{11}|$ is from 854 MHz to 1.02 GHz and from 2.24 to 2.66 GHz. Finally, the antenna was tested inside grey brain matter and it shows a good impedance matching between 0.9 and 1.05 GHz and from 2.27 to 2.73 GHz.

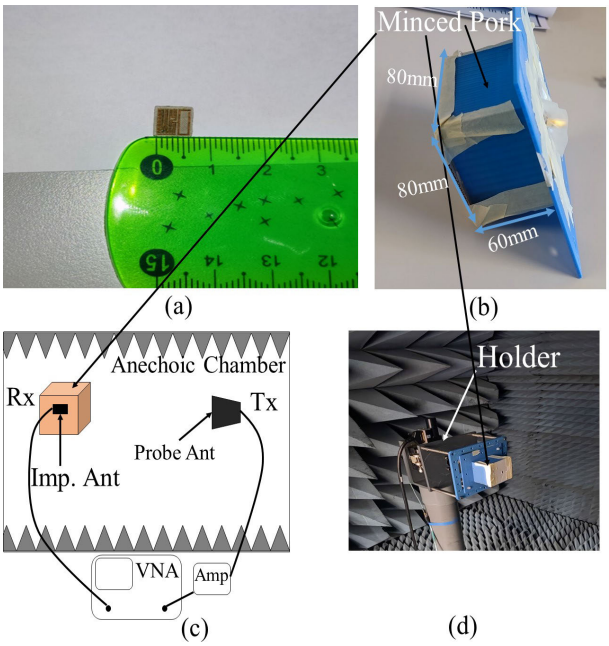

FIGURE 17. (a) Fabrication of the prototype antenna. (b) Minced pork box dimensions. (c) Radiation patterns measurement block diagram. (d) Radiation patterns measurement.

Fig. 17(a) shows the fabricated antenna. Fig. 17(b) shows the proposed antenna inside the 3D minced pork box (The box material is plastic with a permittivity of 2.7). Fig. 17(c) shows the block diagram of the radiation patterns measurement. Fig. 17(d) shows the radiation patterns measurement of the proposed antenna inside minced pork box. To validate the simulated results, the proposed antenna was measured inside minced pork, because pork has similar electrical properties to the human tissue [18]. Fig. 18 shows the measurement setup of the proposed antenna inside minced pork. The $|S_{11}|$ are shown in Fig. 19.

It has been observed a good agreements between simulated and measured $|S_{11}|$. The $|S_{11}|$ below -10 dB is observed from 790 to 940 MHz and from 2.33 to 2.63 GHz (red solid line in Fig. 19).

The proposed antenna shows a gain value of -21 dBi at 915 MHz and -17 dBi at 2.4 GHz. Fig. 20 shows the simulated and measured radiation patterns of the proposed antenna at 915 MHz and 2.4 GHz inside the muscle box.

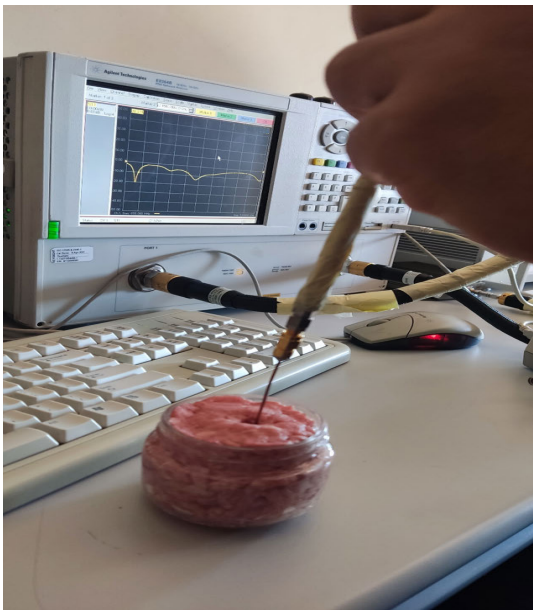

FIGURE 18. Measurement of the prototype antenna inside minced pork.

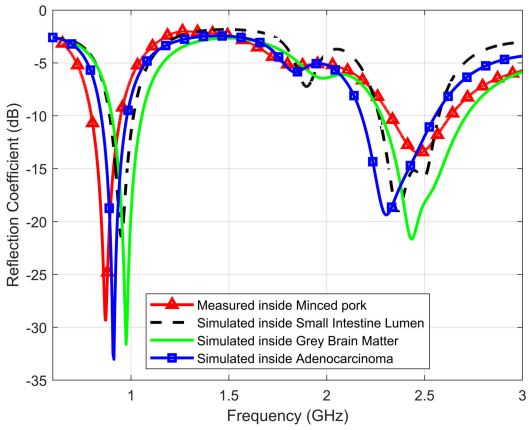

FIGURE 19. Comparison between simulated and measured $|S_{11}|$ inside minced pork.

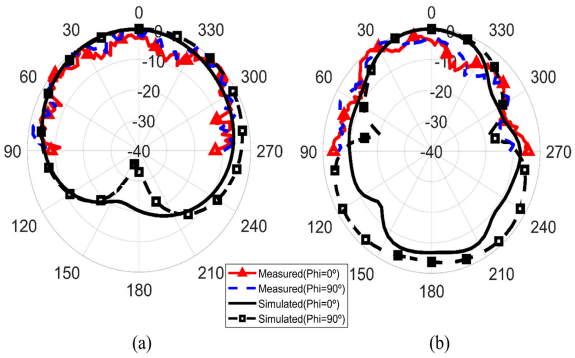

FIGURE 20. Comparison between simulated and measured radiation patterns. (a) 915 MHz. (b) 2400 MHz.

Because of the metallic holder inside the anechoic chamber (Fig. 17(d)) we are only showing the measured radiation

TABLE 5. Comparison of the proposed antenna with recently published literature.

Ref. year	Dim[λ^2]	Freq(MHz)	Bandwidth(%)	Gain(dBi)	Via	Depth(mm)	Adenocarcinoma
[14] 2019	0.02×0.02 0.05×0.05	928 2450	20 8.9	-28.74 -25.65	Yes	50	No
[27] 2020	0.04×0.01 0.09×0.03 0.25×0.08	400 915 2400	236 104 55.4	-29.7 -28.7 -20.8	No	100	No
[28] 2020	0.07×0.07	2400	21.5	-33	Yes	3	No
[29] 2020	0.08×0.08	2450	11.7	-14.6	Yes	4	No
[30] 2018	0.03×0.03	915	8.8	-29	No	4	No
[31] 2019	0.08×0.08	2450	3.2	-25	No	>10	No
[32] 2016	0.02×0.03 0.17×0.18	400 2400	7.4 6.6	-36.7 -27.1	Yes	4	No
[33] 2020	0.02×0.02 0.05×0.05	915 2450	11.7 11.4	-28.94 -23.06	Yes	3	No
[34] 2018	0.02×0.01 0.06×0.05	915 2450	9.8 8.5	-28.5 -22.8	No	4	No
[35] 2019	0.03×0.03 0.08×0.08	920 2450	- -	-29.33 -21	No	2	No
[36] 2020	0.01×0.01 0.07×0.07	400 2450	22.8 13.1	-28.1 -31.3	No	10	No
[37] 2021	0.05×0.05 0.09×0.09	1400 2450	3.1 2.5	-22.06 -21.66	Yes	-	No
[38] 2021	0.168×0.084	2400	8.5	-22	Yes	3	No
[39] 2022	0.02×0.01 0.15×0.05	434 2450	10 22	-28.9 -18.6	No	45.5	No
[40] 2022	0.04×0.04	2400	1038.7	-20.7	Yes	12	No
This Work	**0.01×0.01** **0.04×0.04**	**915** **2400**	**12.6** **12.8**	**-21** **-19**	**No**	45	**Yes**

patterns between −90° and +90°. Good agreement between the simulated and the measured results can be seen.

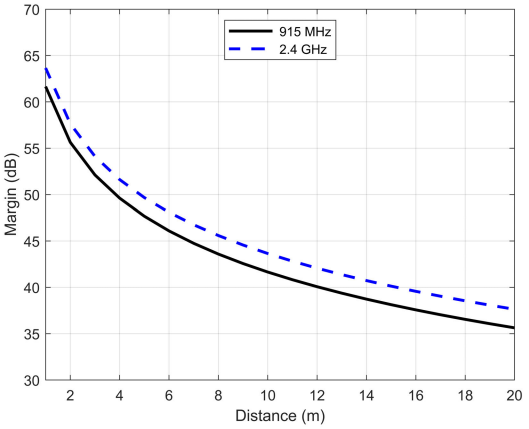

FIGURE 21. Link budget analysis in different resonating frequency.

The link-budget of the proposed antenna has been studied to investigate the feasibility of its usage as an implantable antenna and ensuring good communication with the external device. Given an ideal phase shift keying $\frac{E_b}{N_0} = 9.6$ dB, the Boltzmann's constant K = 1.38 × 10^{-23}, $T_0 = 273$ K is the temperature, and data rate B_r of 78 Mbps. The required power R_p is given by [26]:

$$R_p = \frac{E_b}{N_0} + KT_0 + B_r \tag{5}$$

The available power is defined as [26]:

$$A_p = P_t + G_t + G_r - L_f \tag{6}$$

where $P_t = -4$ dBm is the input transmitter power, $G_r = 2$ dBi is the receiver antenna gain, L_f is the free space loss, and G_t is the proposed implantable antenna gain at the different operating frequency. The link margin is the subtraction of R_p from A_p. It can be clearly seen in Fig. 21 that communication can be ensured in both operating bands at a distance of more than 20 m with a link margin of more than 35 dB.

To ensure patient safety, the specific absorption rate (SAR) has been simulated inside the human head model and small intestine lumen at an incident power of 1 W [41]. Fig. 22 (a) shows the SAR over 1 g inside the human head which is 891 W/kg at 915 MHz and 877 W/kg at 2.4 GHz, that gives an input power of 1.7 mW and 1.8 mW at 915 MHz and 2.4 GHz, respectively. Fig. 22 (b) shows the SAR over

1 g inside the small intestine lumen which is 898 W/kg at 915 MHz and 844 W/kg at 2.4 GHz, that gives an input power of 1.7 mW and 1.8 mW at 915 MHz and 2.4 GHz, respectively. Fig. 22 (c) shows the SAR over 10 g inside the human head which is 92 W/kg at 915 MHz and 95 W/kg at 2.4 GHz, that gives an input power of 17 mW and 16 mW at 915 MHz and 2.4 GHz, respectively. Fig. 22 (d) shows the SAR over 10 g inside the small intestine lumen which is 93 W/kg at 915 MHz and 91 W/kg at 2.4 GHz, that gives an input power of 17 mW at both frequencies. According to [42], the power delivered to the implantable antenna is around 100 μW, which consequent that the proposed antenna respects the IEEE C95.1–1999 (avg SAR<1.6W/Kg at 1 g), and the IEEE C95.1–2005 (avg SAR<2W/Kg at 10 g).

Moreover, Table 6 summarize the SAR values inside grey brain matter, small intestine lumen, stomach, and adenocarcinoma, and it can be concluded that the SAR values satisfy IEEE regulations as reported in [36], [42], and [43].

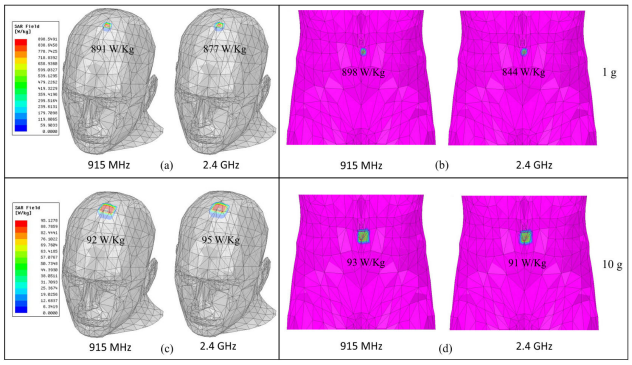

FIGURE 22. Peak SAR analysis (Input power = 1 W) over 1 g inside (a) Human head. (b) Small intestine lumen and over 10 g inside (c) Human head. (d) Small intestine lumen.

TABLE 6. Simulated maximum peak SAR values inside different tissue types.

Tissue model	Frequency	Max SAR (W/Kg)	
		1 g	10 g
Grey Brain Matter	915 MHz	891	92
	2.4 GHz	877	95
Small Intestine Lumen	915 MHz	898	93
	2.4 GHz	844	91
Stomach	915 MHz	935	96
	2.4 GHz	800	87
Adenocarcinoma	915 MHz	939	97
	2.4 GHz	796	87

From Table 5, showing all recently published state-of-the-art related works, it can be seen that the proposed antenna presents the smallest dimension's size, has a full ground plane and the working from the highest and lowest operating band is independent. The proposed antenna has higher bandwidth than the ones in [29], [30], [31], [32], [33], [34], and [37], [38] and higher gain than in [14], [27], [28], [30], [31], [32], [33], [34], [35], [36], [37], [38], and [39]. In addition, it does not use any via, contrary to what is shown in [14], [28], [29], [32], [33], [37], [38], making this design very suitable for biomedical applications.

III. CONCLUSION

In this paper, a dual-band implantable antenna operating at 915 MHz and 2.4 GHz ISM band applications has been presented. The proposed antenna has a small size of ($6 \times 6 \times 0.25$ mm^3), exhibits a bandwidth of 120 MHz at 915 MHz, and 310 MHz at 2.4 GHz. The maximum gain of the antenna is about -21.8 dBi at 915 MHz and -19.2 dBi at 2.4 GHz. Compared with the recently published state of the art, the proposed antenna presents the smallest dimension's size, has a full ground plane, and independency between the highest and lowest operating band making this design very suitable for the biomedical applications. The simulation results were experimentally validated inside minced pork. The proposed implantable antenna shows an ability to communicate at a distance of more than 20 m at 915 MHz and 2.4 GHz.

REFERENCES

[1] A. Kiourti and K. S. Nikita, "A review of in-body biotelemetry devices: Implantables, ingestibles, and injectables," *IEEE Trans. Biomed. Eng.*, vol. 64, no. 7, pp. 1422–1430, Jul. 2017.

[2] H. Bahrami, E. Porter, A. Santorelli, B. Gosselin, M. Popovic, and L. A. Rusch, "Flexible sixteen monopole antenna array for microwave breast cancer detection," in *Proc. 36th Annu. Int. Conf. IEEE Eng. Med. Biol. Soc.*, Aug. 2014, pp. 3775–3778.

[3] I. A. Shah, M. Zada, and H. Yoo, "Design and analysis of a compact-sized multiband spiral-shaped implantable antenna for scalp implantable and leadless pacemaker systems," *IEEE Trans. Antennas Propag.*, vol. 67, no. 6, pp. 4230–4234, Jun. 2019.

[4] A.-M. Bouvier, M. Robaszkiewicz, V. Jooste, M. Cariou, A. Drouillard, V. Bouvier, and J.-B. Nousbaum, "Trends in incidence of small bowel cancer according to histology: A population-based study," *J. Gastroenterol.*, vol. 55, no. 2, pp. 181–188, Feb. 2020.

[5] M. Guardiola, S. Buitrago, G. Fernández-Esparrach, J. M. O'Callaghan, J. Romeu, M. Cuatrecasas, H. Córdova, M. Á. G. Ballester, and O. Camara, "Dielectric properties of colon polyps, cancer, and normal mucosa: Ex vivo measurements from 0.5 to 20 GHz," *Med. Phys.*, vol. 45, no. 8, pp. 3768–3782, Aug. 2018.

[6] A. Basir, M. Zada, and H. Yoo, "Compact and flexible wideband antenna for intraoral tongue-drive system for people with disabilities," *IEEE Trans. Antennas Propag.*, vol. 68, no. 3, pp. 2405–2409, Mar. 2020.

[7] L.-J. Xu, J.-P. Xu, Z.-J. Chu, S. Liu, and X. Zhu, "Circularly polarized implantable antenna with improved impedance matching," *IEEE Antennas Wireless Propag. Lett.*, vol. 19, pp. 876–880, 2020.

[8] T. Karacolak, A. Z. Hood, and E. Topsakal, "Design of a dual-band implantable antenna and development of skin mimicking gels for continuous glucose monitoring," *IEEE Trans. Microw. Theory Techn.*, vol. 56, no. 4, pp. 1001–1008, Apr. 2008.

[9] S. Bakogianni and S. Koulouridis, "A dual-band implantable rectenna for wireless data and power support at sub-GHz region," *IEEE Trans. Antennas Propag.*, vol. 67, no. 11, pp. 6800–6810, Nov. 2019.

[10] W. H. Ko, "Early history and challenges of implantable electronics," *ACM J. Emerg. Technol. Comput. Syst.*, vol. 8, no. 2, pp. 1–9, Jun. 2012.

[11] A. Lamkaddem, A. E. Yousfi, L. E. G. Muñoz, and D. Segovia-Vargas, "A compact wideband circularly polarized implantable antenna for cardiac pacemaker devices," in *Proc. Int. Conf. Electromagn. Adv. Appl. (ICEAA)*, Aug. 2021, pp. 379–382.

[12] X. Y. Liu, Z. T. Wu, Y. Fan, and E. M. Tentzeris, "A miniaturized CSRR loaded wide-beamwidth circularly polarized implantable antenna for subcutaneous real-time glucose monitoring," *IEEE Antennas Wireless Propag. Lett.*, vol. 16, pp. 577–580, 2017.

[13] W. Cui, R. Liu, L. Wang, M. Wang, H. Zheng, and E. Li, "Design of wideband implantable antenna for wireless capsule endoscope system," *IEEE Antennas Wireless Propag. Lett.*, vol. 18, pp. 2706–2710, 2019.

[14] F. Faisal and H. Yoo, "A miniaturized novel-shape dual-band antenna for implantable applications," *IEEE Trans. Antennas Propag.*, vol. 67, no. 2, pp. 774–783, Feb. 2019.

[15] M. Zada, I. A. Shah, and H. Yoo, "Metamaterial-loaded compact high-gain dual-band circularly polarized implantable antenna system for multiple biomedical applications," *IEEE Trans. Antennas Propag.*, vol. 68, no. 2, pp. 1140–1144, Feb. 2020.

[16] M. Yousaf, I. B. Mabrouk, F. Faisal, M. Zada, Z. Bashir, A. Akram, M. Nedil, and H. Yoo, "Compacted conformal implantable antenna with multitasking capabilities for ingestible capsule endoscope," *IEEE Access*, vol. 8, pp. 157617–157627, 2020.

[17] A. Lamkaddem, A. El Yousfi, K. A. Abdalmalak, V. G. Posadas, L. E. G. Muñoz, and D. Segovia-Vargas, "A compact design for dual-band implantable antenna applications," in *Proc. 15th Eur. Conf. Antennas Propag. (EuCAP)*, Mar. 2021, pp. 1–3.

[18] Z. Z. Abidin, F. N. Omar, D. R. A. Biak, and Y. C. Man, "Alternative for rapid detection and screening of pork, chicken, and beef using dielectric properties in the frequency of 0.5 to 50 GHz," *Int. J. Food Properties*, vol. 19, no. 5, pp. 1127–1138, May 2016, doi: 10.1080/10942912.2015.1058274.

[19] K. Zhang, C. Liu, X. Liu, H. Cao, Y. Zhang, X. Yang, and H. Guo, "A conformal differentially fed antenna for ingestible capsule system," *IEEE Trans. Antennas Propag.*, vol. 66, no. 4, pp. 1695–1703, Apr. 2018.

[20] S. Gabriel, R. W. Lau, and C. Gabriel, "The dielectric properties of biological tissues: III. Parametric models for the dielectric spectrum of tissues," *Phys. Med. Biol.*, vol. 41, no. 11, pp. 2271–2293, Nov. 1996.

[21] G. Stojanović, L. Živanov, and M. Damnjanović, "Novel efficient methods for inductance calculation of meander inductor," *Int. J. Comput. Math. Electr. Electron. Eng.*, vol. 25, no. 4, pp. 916–928, Oct. 2006.

[22] S. S. Mohan, M. del Mar Hershenson, S. P. Boyd, and T. H. Lee, "Simple accurate expressions for planar spiral inductances," *IEEE J. Solid-State Circuits*, vol. 34, no. 10, pp. 1419–1424, Oct. 1999.

[23] G. Stojanovic, M. Damnjanovic, V. Desnica, L. Zivanov, R. Raghavendra, P. Bellew, and N. Mcloughlin, "High-performance zig-zag and meander inductors embedded in ferrite material," *J. Magn. Magn. Mater.*, vol. 297, no. 2, pp. 76–83, Feb. 2006.

[24] C. Saha and J. Y. Siddiqui, "Versatile CAD formulation for estimation of the resonant frequency and magnetic polarizability of circular split ring resonators," *Int. J. RF Microw. Comput.-Aided Eng.*, vol. 21, no. 4, pp. 432–438, Jul. 2011.

[25] F. E. Terman, *Radio Engineers' Handbook*, vol. 1, no. 9. New York, NY, USA: McGraw-Hill, 1950, p. 4.

[26] M. Zada, I. A. Shah, J. Nasir, A. Basir, and H. Yoo, "Empowering remote patient monitoring with a dual-band implantable rectenna system for wireless power and data transfer," *IEEE Trans. Antennas Propag.*, vol. 71, no. 12, pp. 9509–9522, Dec. 2023.

[27] A. Basir, M. Zada, Y. Cho, and H. Yoo, "A dual-circular-polarized endoscopic antenna with wideband characteristics and wireless biotelemetric link characterization," *IEEE Trans. Antennas Propag.*, vol. 68, no. 10, pp. 6953–6963, Oct. 2020.

[28] Z. Xia, H. Li, Z. Lee, S. Xiao, W. Shao, X. Ding, and X. Yang, "A wideband circularly polarized implantable patch antenna for ISM band biomedical applications," *IEEE Trans. Antennas Propag.*, vol. 68, no. 3, pp. 2399–2404, Mar. 2020.

[29] G. Samanta and D. Mitra, "Miniaturised and radiation efficient implantable antenna using reactive impedance surface for biotelemetry," *IET Microw., Antennas Propag.*, vol. 14, no. 2, pp. 177–184, Feb. 2020.

[30] C. Liu, Y. Zhang, and X. Liu, "Circularly polarized implantable antenna for 915 MHz ISM-band far-field wireless power transmission," *IEEE Antennas Wireless Propag. Lett.*, vol. 17, pp. 373–376, 2018.

[31] B. Rana, J.-Y. Shim, and J.-Y. Chung, "An implantable antenna with broadside radiation for a brain–machine interface," *IEEE Sensors J.*, vol. 19, no. 20, pp. 9200–9205, Oct. 2019.

[32] Y. Liu, Y. Chen, H. Lin, and F. H. Juwono, "A novel differentially fed compact dual-band implantable antenna for biotelemetry applications," *IEEE Antennas Wireless Propag. Lett.*, vol. 15, pp. 1791–1794, 2016.

[33] F. Faisal, M. Zada, A. Ejaz, Y. Amin, S. Ullah, and H. Yoo, "A miniaturized dual-band implantable antenna system for medical applications," *IEEE Trans. Antennas Propag.*, vol. 68, no. 2, pp. 1161–1165, Feb. 2020.

[34] S. A. A. Shah and H. Yoo, "Scalp-implantable antenna systems for intracranial pressure monitoring," *IEEE Trans. Antennas Propag.*, vol. 66, no. 4, pp. 2170–2173, Apr. 2018.

[35] G. Samanta and D. Mitra, "Dual-band circular polarized flexible implantable antenna using reactive impedance substrate," *IEEE Trans. Antennas Propag.*, vol. 67, no. 6, pp. 4218–4223, Jun. 2019.

[36] Y. Fan, H. Liu, X. Liu, Y. Cao, Z. Li, and M. M. Tentzeris, "Novel coated differentially fed dual-band fractal antenna for implantable medical devices," *IET Microw., Antennas Propag.*, vol. 14, no. 2, pp. 199–208, Feb. 2020. [Online]. Available: https://digital-library.theiet.org/content/journals/10.1049/iet-map.2018.6171

[37] A. Valanarasi and R. Dhanasekaran, "Optimum band E shaped miniature implantable antennas for telemetry applications," *IEEE Trans. Antennas Propag.*, vol. 69, no. 1, pp. 55–63, Jan. 2021.

[38] M. S. Singh, J. Ghosh, S. Ghosh, and A. Sarkhel, "Miniaturized dual-antenna system for implantable biotelemetry application," *IEEE Antennas Wireless Propag. Lett.*, vol. 20, pp. 1394–1398, 2021.

[39] D. Nikolayev, A. K. Skrivervik, J. S. Ho, M. Zhadobov, and R. Sauleau, "Reconfigurable dual-band capsule-conformal antenna array for in-body bioelectronics," *IEEE Trans. Antennas Propag.*, vol. 70, no. 5, pp. 3749–3761, May 2022.

[40] N. Abbas, S. A. A. Shah, A. Basir, Z. Bashir, A. Akram, and H. Yoo, "Miniaturized antenna for high data rate implantable brain-machine interfaces," *IEEE Access*, vol. 10, pp. 66018–66027, 2022.

[41] S. Hayat, A. Basir, and H. Yoo, "Modeling and in vitro measurement of a compact antenna for intravascular catheter tracking and imaging system," *IEEE Trans. Instrum. Meas.*, vol. 72, pp. 1–14, 2023.

[42] A. Lamkaddem, A. E. Yousfi, K. A. Abdalmalak, V. G. Posadas, and D. Segovia-Vargas, "Circularly polarized miniaturized implantable antenna for leadless pacemaker devices," *IEEE Trans. Antennas Propag.*, vol. 70, no. 8, pp. 6423–6432, Aug. 2022.

[43] Z. Hamouda, J.-L. Wojkiewicz, A. A. Pud, L. Koné, S. Bergheul, and T. Lasri, "Magnetodielectric nanocomposite polymer-based dual-band flexible antenna for wearable applications," *IEEE Trans. Antennas Propag.*, vol. 66, no. 7, pp. 3271–3277, Jul. 2018.

ABDENASSER LAMKADDEM was born in El Aioun Sidi Mellouk, Morocco, in 1993. He received the B.S. degree from Mohamed I University, Oujda, Morocco, in 2014, and the M.S. degree in communication systems and embedded electronics from Abdelmalek Essaadi University, Tangier, Morocco, in 2016. He is currently pursuing the Ph.D. degree with the Carlos III University of Madrid (UC3M), Madrid, Spain.

In 2019, he was a Visiting Student with the Department of Signal Theory and Communications, UC3M. In 2023, he was a Visiting Research Student with the Electrical and Electronic Engineering Department, University of Liverpool, Liverpool, U.K. He has authored/coauthored several international conference papers and journal articles. He has participated in several research projects financed by Telnet and Huawei. His research interests include implantable, wearable antennas and wireless power transfer for biomedical applications, small antennas, antenna arrays for 5G applications, ultra-wideband antennas, reconfigurable antennas, EBG, frequency selective surfaces, and characteristic mode analysis.

Mr. Lamkaddem received the Erasmus+ Grant, in 2019. He has served as a Peer-Reviewer for IEEE Access and *International Journal of Communication Systems* (IJCS).

AHMED EL YOUSFI was born in Al Hoceima, Morocco. He received the dual bachelor's degree in physics from the University of Lille 1 Sciences and Technology, Villeneuve-d'Ascq, France, and Mohamed I University, Oujda, Morocco, in 2016, and the master's degree in electronics and telecommunications engineering from Abdelmalek Essaadi University, Tetouan, Morocco, in 2017. He is currently pursuing the Ph.D. degree with the Group of Radiofrequency, Electromagnetics, Microwaves and Antennas (GREMA), Carlos III University of Madrid (UC3M), Madrid, Spain.

In 2020, he joined the Signal Theory and Communications Department, UC3M, as a Teaching Assistant. He worked on Massive MIMO antennas for Huawei project and Ferrite antennas for Indra. In 2022, he was a Visiting Ph.D. Student with the Department of Electrical and Information Technology, Lund University, Lund, Sweden. He has authored/coauthored several international conference papers and journal articles. His research interests include multiband/broadband antennas based on metamaterials, characteristic mode analysis for metasurface antennas, array antennas for 5G applications, and implantable antennas.

Mr. Yousfi received the Erasmus+ Grant in 2019. He has served as a Peer-Reviewer for IEEE Access and the European Conference on Antennas and Propagation (EuCAP).

VICENTE GONZÁLEZ-POSADAS was born in Madrid, Spain, in 1968. He received the B.S. degree in radio communication engineering from Universidad Politécnica de Madrid (UPM), Madrid, in 1992, the M.S. degree in physics from the National University of Distance Education, Madrid, in 1995, the master's degree in high strategic studies from CESEDEN (organization pertaining to the Spanish Ministry of Defense), Madrid, in 2009, and the Ph.D. degree in telecommunication engineering from the Carlos III University of Madrid, Madrid, in 2001. He is currently a Full Professor with the Technical Telecommunications School, UPM. He has authored or coauthored more than 100 technical conference, letter, and journal papers. His current research interests include MMICs, active antennas, microstrip antennas, CRLH lines and metamaterials, microwave technology, and RFID.

DANIEL SEGOVIA-VARGAS (Senior Member, IEEE) was born in April 1968. He received the Ph.D. degree and the Ph.D. degree (cum laude) in telecommunications engineering from ETSIT, Universidad Politécnica de Madrid (UPM), Madrid, Spain, in 1993 and 1998, respectively, and the Doctor Honoris Causa degree from Universidad Católica San Pablo, Arequipa, Peru, in 2019.

From 1993 to 1998, he was an Assistant Professor with Universidad de Valladolid, Valladolid, Spain. Since 1998, he has been a Professor with Universidad Carlos III de Madrid (UC3M), Madrid. Since 2001, he has been an Associate Professor (a Tenure) of signal theory and communications at the signals with UC3M, where he is currently teaching high-frequency microwave and circuits and antennas. Since 2003, he has been chairing the Group of Radiofrequency, Electromagnetics, Microwaves and Antennas (GREMA), UC3M. From 2004 to 2010, he was the Head of Telecommunications Engineering of Escuela Politécnica Superior, UC3M. From 2012 to November 2020, he was the Head of Escuela Politécnica Superior, UC3M. He has been a Full Professor with UC3M, since 2016. He has been a Visiting Researcher with the Rutherford Appleton Laboratory, Didcot, U.K., and Czech Technical University in Prague, Prague, Czechia. He has authored or coauthored more than 350 publications in scientific journals and international conferences (more than 90 in indexed international journals and more than 20 international invited conferences). His research interests include antennas (antenna arrays and miniaturized antennas, where he has led different projects with outstanding companies, such as Airbus, Repsol, or Indra), active antennas, metamaterials, and technologies in THz frequencies.

Prof. Segovia-Vargas was a member of the Organizing Committee of EuCAP 2010 (where he was the Awards Committee). He has been a member of the AP-S Society, since 1998, and the MTT-S Society, since 2001. He received the Best Thesis Award in Mobile Communication by COIT-Ericsson for the Ph.D. degree. He was the Chairperson of URSI2011. He has organized several international workshops in the domain of metamaterials and THz technologies. He has chaired more than 80 research and development projects, both public and private. He has been chairing courses in the European School of Antennas, since 2013. He has been the National Delegate of European Cost actions in the antennas field (Cost 284, Cost IC0603, and Cost IC1102), since 2002. Since 2013, he has been a Treasurer and a Secretary of the IEEE Spanish Chapter. He has been the Treasurer of the European Microwave Conference, since 2018, and EuCAP 2022, Madrid.